International Journal of Nanomedicine

Dovepress
open access to scientific and medical research

Open Access Full Text Article

ORIGINAL RESEARCH

Short-Wavelength Aggregation-Induced Emission Photosensitizers for Solid Tumor Therapy: Enhanced with White-Light Fiber Optic

Zijuan Meng[1], Zhaojun Chen[1], Guangwen Lu[1], Xiaoqi Dong[1], Jun Dai[2], Xiaoding Lou[1], Fan Xia[1]

[1]Faculty of Materials Science and Chemistry, China University of Geosciences, Wuhan, 430074, People's Republic of China; [2]Department of Obstetrics and Gynecology, Tongji Hospital, Tongji Medical College, Huazhong University of Science and Technology, Wuhan, 430034, People's Republic of China

Correspondence: Jun Dai, Department of Obstetrics and Gynecology, Tongji Hospital, Tongji Medical College, Huazhong University of Science and Technology, Wuhan, 430034, People's Republic of China, Email dj_hust1987@sina.com; jundai@tjh.tjmu.edu.cn

Background: White-light photodynamic therapy (wPDT) has been used in the treatment of cancer due to its convenience, effectiveness and less painful. However, the limited penetration of white-light into the tissues leads to a reduced effectiveness of solid tumor treatment.

Methods: Two short-wavelength aggregation-induced emission (AIE) nanoparticles were prepared, PyTPA@PEG and TB@PEG, which have excitation wavelengths of 440 nm and 524 nm, respectively. They were characterized by UV, fluorescence, particle size and TEM. The ability of nanoparticles to produce reactive oxygen species (ROS) and kill cancer cells under different conditions was investigated in vitro, including white-light, after white-light penetrating the skin, laser. A white-light fiber for intra-tumor irradiation was customized. Finally, induced tumor elimination with fiber-mediated wPDT was confirmed in vivo.

Results: In vitro, both PyTPA@PEG and TB@PEG are more efficient in the production ROS when exposed to white-light compared to laser. However, wPDT also has a fatal flaw in that its level of ROS production after penetrating the skin is reduced to 20–40% of the original level. To this end, we have customized a white-light fiber for intra-tumor irradiation. In vivo, the fiber-mediated wPDT significantly induces tumor elimination with maximized therapeutic outcomes by irradiating the interior of the tumor. In addition, wPDT also has the advantage that its light source can be adapted to a wide range of photosensitizers (wavelength range 400–700 nm), whereas a laser of single wavelength can only target a specific photosensitizer.

Conclusion: This method of using optical fiber to increase the tissue penetration of white light can greatly improve the therapeutic effect of AIE photosensitizers, which is needed for the treatment of large/deep tumors and holds great promise in cancer treatment.

Keywords: aggregation-induced emission, photodynamic therapy, photosensitizer, white light, fiber optic

Introduction

Cancer ranks as a leading cause of death and a major obstacle to improving life expectancy in countries around the world.[1,2] To inhibit the rapid growth of tumors, the advanced treatments such as chemotherapy, gene therapy, photothermal therapy, immune therapy and photodynamic therapy (PDT) have emerged, among which PDT is a medical treatment that uses photosensitizers in combination with a specific light source to generate reactive oxygen species (ROS), thus exerting cytotoxic activity in tumor cells.[3–11] To date, PDT has been established as a safe modality for ablating many types of tumors because of its noninvasive procedure, enhanced tumor selectivity and good cosmetic outcomes.[12–15] With a large amount of recent technological advances, PDT is capable of becoming mainstream of cancer treatment.[16]

Photosensitizers (PS), oxygen and light are the three components in PDT.[17] In order to obtain the best curative effect of cancer therapy, the PSs bearing high photodynamic abilities are key to their efficacy. ROS is the key to killing cancer cells such as radicals and singlet species ($^1O_2$) are generated mainly through the exciton that react with surrounding molecules or oxygen, undergo the intersystem crossover (ISC) process to form the triplet excited states.[18–22] However,

Received: 29 July 2022
Accepted: 9 December 2022
Published: 22 December 2022

traditional photosensitizers easily aggregate in aqueous phase, resulting in aggregation-induced quenching (ACQ) and ROS production efficiency reduction, thus the application has been greatly affected.[23–25] Fortunately, the aggregation-induced emission luminogens (AIEgens) was discovered by Tang's team, which not only exhibited stronger enhanced emissivity than monomers when aggregated, to solve the problem of ACQ, but also facilitated cancer treatment due to its high ROS generation efficiency.[26–30] Benefiting from many AIE-based photosensitizers have been successfully designed and presented, which largely block non-radiative pathways while promoting both radiative pathways and ISC processes, further enhancing ROS production.[31–37] In addition, photobleaching has no significant effect on the ROS production capacity of AIEgens, but photosensitivity of traditional photosensitizers such as Ce6 is greatly reduced after photobleaching.[38,39] Furthermore, AIEgens has other additional memorable features, including the distinguishable emission from the visible to near-infrared region, photothermal conversion and fluorescence sensing based on assembly or disassembly.[40–46] Therefore, AIE-based photosensitizers can be applicable for imaging and therapeutic functions, while making it a choice for clinical with excellent potential.

PS is excited by specific wavelengths, including laser and white light. Therefore, the choice of light source and application mode is one of the parameters that must be considered. Through the application of high-power laser focus in clinical practice, it has a certain therapeutic effect on surface tumors and precancerous lesions, and causes less trauma to patients.[47] However, laser therapy for tumour ablation has important limitations, including the non-selectivity and the requirement for a high-power density up to hundreds of watts, which introduces safety and logistical issues.[48] At the same time, the discomfort and pain during and after treatment impede its usage.[49] White light emits 400–700 nm wavelength which covers the absorption peaks of most available photosensitizers nowadays, improving the non-selectivity of photosensitizer. Owing to efficient light absorption of the PS, white light enables phototherapy using lower power densities. Patients experienced less pain and more satisfactory safety during treatment.[50] In addition, white light sources are safer for the human body and easier to manage than laser instruments. Currently, inorganic-PSs as well as basic organic small molecules, such as carbon dots and Au nanoclusters, have been applied to treat cancer in the context of white-light PDT (wPDT).[51–56] Regrettably, wPDT also has a fatal flaw in that the depth of tissue penetration of white-light is limited.[57] When light enters tissue, it scatters or absorbs; the degree to which either process occurs depends on the kind of tissue and the wavelength of the light.[58] In terms of wavelength, 630 nm is most frequently employed in clinical settings for PDT, the penetration depth of the long-wavelength red light is only 1–3 mm, which fails to meet the requirement of the treatment of solid or deep-seated tumors.[59] In the wavelength range of white light, the penetration depth of light is not superior. Therefore, the use of light delivery paradigms in oncology clinical phototherapy is needed to treat large and/or deep tumors.

Here, two short-wavelength AIE photosensitizers were successfully prepared and nanosized using PEG-DSPE and named PyTPA@PEG and TB@PEG, respectively. PyTPA@PEG and TB@PEG have UV absorption maxima of 440 nm and 524 nm, respectively. In vitro, PyTPA@PEG and TB@PEG have powerful photosensitizing effects and are superior in anti-photobleaching, killing tumor cells rapidly and effectively under the irradiation of white light. However, for deep tumors, this AIE photosensitizer is inadequate due to the limited penetration depth of white light. For this purpose, we have developed a delivery device for white light, which is capable of delivering white light into the tumor for PDT, thereby inhibiting tumor growth. This highly effective short-wavelength AIE photosensitizer, used by incorporating white light fiber, is a simple and effective strategy that offers new horizons for the clinical application of short-wavelength photosensitizers.

Experimental Section

Materials

Dimethylsulfoxide (DMSO) and tetrahydrofuran (THF) were purchased from China National Medicines Co. Ltd. 1,2-distearoyl-sn-glycero-3-phosphoethanolamine-N [methoxy (polyethylene glycol)-2000] (PEG-DSPE) was purchased from Xi'an Ruixi Biological Technology Co. Ltd. Phosphate buffered saline (PBS), fetal bovine serum (FBS), trypsin, Dulbecco's Modified Eagle's Medium (DMEM) and penicillin−streptomycin were purchased from Gibco Invitrogen Corporation. 9.10-Anthracenediyl-bis(methylene)dim alonic acid (ABDA) was provided by Sigma-Aldrich.

2.7-dichlorodihydrofluorescein diacetate (DCFH-DA), 5-chloromethyl fluorescein diacetate (CMFDA) and propidium iodide (PI) were provided by Yeasen Co., Ltd. HeLa cells were purchased from Procell Life Science&Technology Co., Ltd.

Instruments

High-resolution mass spectra (HRMS) was obtained on a Thermo Scientific Q Exactive mass spectrometer system. Fluorescence spectra was taken on an Edinburgh FS5 Fluorescence Spectrophotometer. All UV-Vis absorption was performed on a Shimadzu UV-2600 spectrometer. Hydrodynamic size was determined by a Malvern Instruments Zetasizer Nano ZS90. Transmission electron microscope (TEM) images were taken on a Thermo Fisher Scientific F200x TEM instrument. Confocal images were recorded on a Zeiss LSM 880 confocal laser scanning microscope. Mice and organs were imaged by a small animal imaging system at the PerkinElmer Institute.

Preparation of PyTPA@PEG and TB@PEG Nanoparticles

PyTPA (0.72 mg) and DSPE-PEG2000 (2 mg) were both dissolved in THF (1 mL). The solution was mixed, and ultrasound was performed for 5 min and quickly injected into 10 mL of deionized water in an ultrasonic environment. It was then stirred in fume hood at 700 rpm for one day to volatilize the THF. The crude NPs were further filtered through a membrane filter of 200 nm in diameter and stored at 4°C for further usage. TB@PEG NPs were prepared in the same way as PyTPA@PEG.

Transmission Electron Microscope (TEM)

Morphology of PyTPA@PEG and TB@PEG NPs were observed by TEM. All samples were prepared as 10 μM in H_2O. Dropped the sample on the copper wire and remove the excess liquid with a piece of filter paper after 1 minute.

ROS Generation in Solution

The ROS generated from PyTPA@PEG and TB@PEG NPs were studied by using 9.10-Anthracenediyl-bis(methylene) dim alonic acid (ABDA) as the ROS indicator. PyTPA@PEG NPs were prepared as 5 μM in H_2O. After exposing the solution of PyTPA@PEG to a white light, 532 nm laser or white light penetrating the skin for different time, the spectra at 378 nm was recorded immediately to obtain the decay rate of the photosensitizing process. The experiment of TB@PEG NPs was the same as that of PyTPA@PEG NPs.

Anti-Photobleaching

PyTPA@PEG NPs, TB@PEG NPs and RB were prepared as 5 μM in H_2O. The prepared solution was placed under 100 mW cm^{-2} white light for 30 min, and then ROS in the solution was detected with the light intensity of 80 mW cm^{-2}.

Cell Culture

HeLa cancer cell line was cultured in high glucose Dulbecco's Modified Eagle Medium (DMEM) with 10% FBS and 1% PS in a culture flask at 37°C in a humidified atmosphere containing 5% CO_2.

Cellular Uptake and Intracellular ROS Generation

HeLa cells were seeded in confocal culture dish at a density of 1×10^4 cells. They were cultured for 24 h and then treated with PyTPA@PEG (10 μM) and TB@PEG NPs (10 μM), respectively. After different hours of incubation at 37°C, cell samples were washed with PBS for three times and visualized under a CLSM. The intracellular ROS generation of PyTPA@PEG and TB@PEG NPs were detected using 2.7-dichlorodihydrofluorescein diacetate (DCFH-DA), which was a reactive oxygen species assay. After incubated with PyTPA@PEG (10 μM) for 4 h at 37°C, the cells were washed with PBS and then DCFH-DA (10 μM) was added into the wells for 30 min. The cells were irradiated under different light for 3 min, including white light (200 mW cm^{-2}), 532 nm laser (200 mW cm^{-2}) and white light penetrating the skin. Finally, the cell images were taken by CLSM. Intracellular ROS production of TB@PEG NPs was detected in the same way as

that of PyTPA@PEG NPs. The difference is that Hela cells were incubated with TB@PEG NPs for 24 hours and irradiated under different light for 5 min.

CMFDA and PI Staining

HeLa cells were seeded in confocal culture dish at a density of 1×10^4 cells and incubated for 24 h. The cells were incubated with PyTPA@PEG NPs (20 μM) in fresh medium for 4 h. Then the cells were irradiated under different light for 3 minutes and placed back into the incubator for incubation for 4 hours. About 10 μL CMFDA (1 mM) and 10 μL PI (50 μg mL^{-1}) were added to 1mL cell culture medium, then mixed evenly and cultured in the incubator at 37°C for 30 min. In the end, the medium was removed and the cells were washed with PBS for three times before the CLSM was used for imaging. The experiment of TB@PEG NPs was the similar to that at PyTPA@PEG NPs, but the cells were incubated for 24 hours at a concentration of 30 μM and then illuminated for 5 minutes.

Hemolysis Test

Hemolytic activities of PyTPA@PEG and TB@PEG NPs were evaluated based on haemoglobin released from mouse blood cells. About 1 mL red blood cell (4%) suspension mixed with 0.1 mL PBS served as negative control (no hemolysis) and 0.1 mL H_2O as positive control (100% hemolysis). PyTPA@PEG and TB@PEG NPs of PBS solution (0.1 mL) were added into the mixture of 1 mL red blood cell suspension. The ultimate nanoparticle concentrations were 5 μM, 10 μM, 20 μM and 30 μM, respectively. After 6 h storage at 37°C in dark environment, the samples were centrifuged. Uv absorption was measured using a microplate reader and the hemolysis ratio was calculated according to the following formula: Hemolysis (%) = $(A_{sample} - A_{negative})/(A_{positive} - A_{negative}) \times 100\%$.

Animals and Hela Tumor-Bearing Mouse Model

The experimental animal studies were approved by the Animal Ethics Committee in Tongji Hospital, Tongji Medical College, Huazhong University of Science and Technology, and strictly complied with the requirements of the animal ordinance. Laboratory animal-Guideline for ethical review of animal welfare (GB/T 35892–2018) was strictly observed during the experiment. Eight-week-old nude mice were purchased from Beijing Vital River Laboratory Animal Technology Co. Ltd. (Beijing, China). All mice were fed normally and provided unlimited access to water in a room with 25°C. 5×10^6 Hela cells were inoculated subcutaneously in mice and the tumor volume was measured by vernier caliper and calculated as: volume = (tumor length) × (tumor width) × (tumor width)/2.

In vivo Circulation

TB@PEG NPs (0.5 mg mL^{-1}, 100 μL) was injected into normal mice by tail vein. At 0.1, 0.5, 1, 2, 4, 8, 12, 24, 48 h after TB@PEG NPs injection, 5 μL blood was collected from mice through tail vein and placed in EP tube, and 60 μL PBS was added to mix. Samples were stored at 4°C, and fluorescence imaging was performed by small animal imaging system after all samples were collected. The fluorescence intensity was analyzed by a semi-quantitative biodistribution analysis method. The same operation process as TB@PEG NPs was used in the study of PyTPA@PEG NPs.

In vivo Fluorescence Imaging and Biodistribution

In vivo fluorescence imaging of PyTPA@PEG and TB@PEG NPs were performed in Hela tumor-bearing mice. When the tumor grew to ~200 mm^3, TB@PEG NPs (0.5 mg mL^{-1}, 100 μL) was injected through the tail vein of mice. Subsequently, in vivo fluorescence imaging of photosensitizer NPs was performed at different injection time. PyTPA@PEG was studied in the same way as TB@PEG. For tissue distribution studies, at 48 h after injection, the subcutaneous tumor was removed and organs (heart, liver, spleen, lung and kidneys) were resected from the mice. After that, tumor and organs were imaged again by fluorescence imaging to study the TB@PEG NPs distribution.

Photodynamic Therapy in vivo

The phototherapeutic effects of PyTPA@PEG and TB@PEG NPs were tested in Hela tumor-bearing mice, as well as the effect of optical fiber on tumor treatment. To put it simply, the mice were divided into 5 groups, including PBS group, TB@PEG (I-L), PyTPA@PEG (I-L), TB@PEG (E-L) and PyTPA@PEG (E-L). The treatment was started when the tumor volume was about 80 mm^3, and the treatment process is shown in Figure 1A. PyTPA@PEG or TB@PEG NPs (0.5 mg mL^{-1}, 150 μL) was injected through the tail vein of mice. After 24 h of injection, the tumor was irradiated by a white light (100 mW cm^{-2}, 20 min). Tumor volume and body weight of mice in each group were monitored.

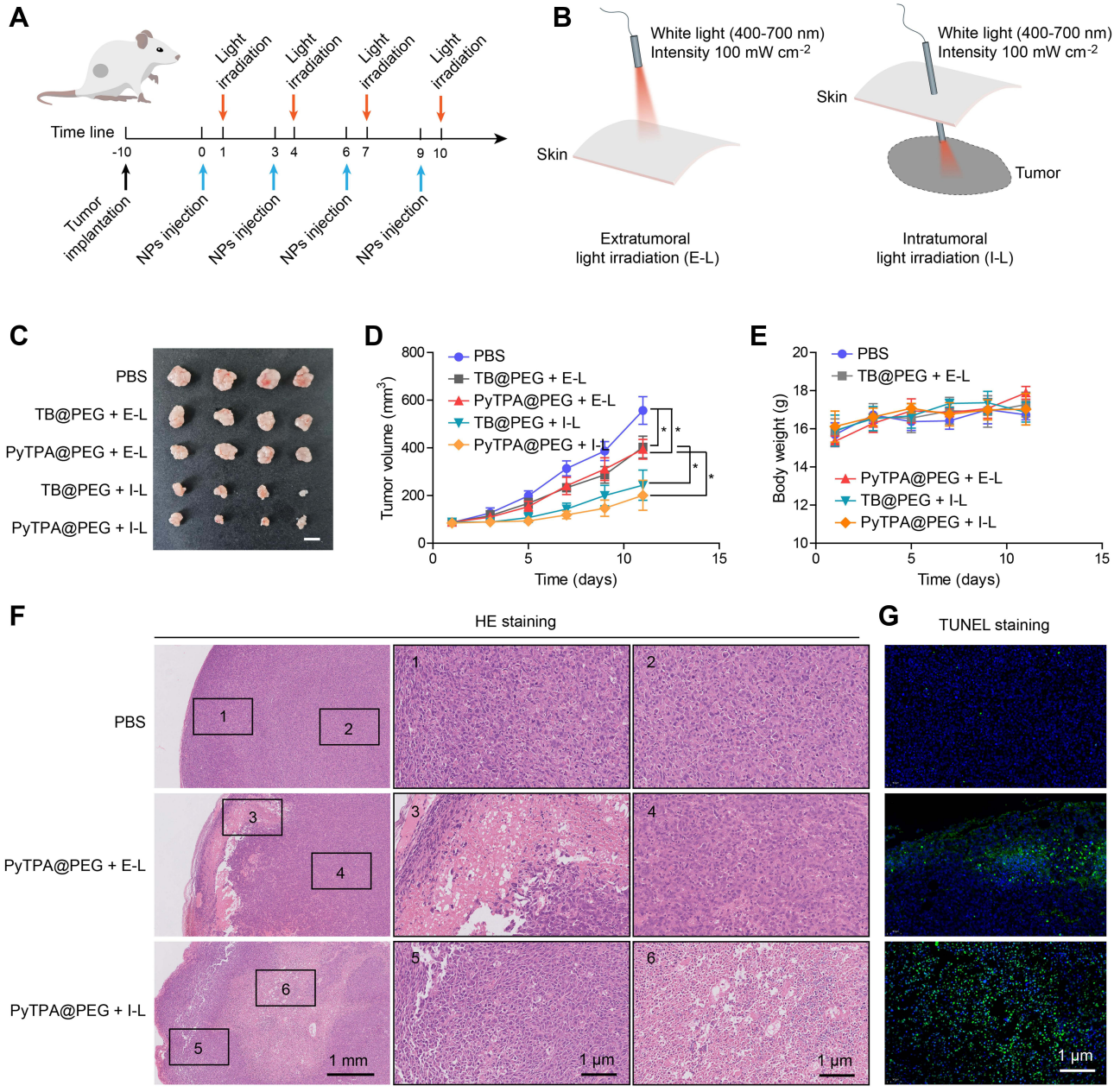

Figure 1 (**A**) The objective to construct Hela subcutaneous tumor and the treatment process. (**B**) Schematic illustrating treatment by extratumoral light irradiation (E-L) or intratumoral light irradiation (I-L). Light intensity:100 mW cm^{-2}, time: 20 min. (**C**) Representative tumor images of the different groups after treatment. (**D**) Growth kinetic curves of tumors in tumor-bearing mice after receiving PyTPA@PEG or TB@PEG -mediated extratumoral light irradiation (E-L) or intratumoral light irradiation (I-L). The data were reported as mean ± SD (n = 4) and analyzed by unpaired *t*-test. * $p < 0.05$. (**E**) Body weight changes in mice during treatment. (**F**) The histological changes of tumors were observed by H&E staining. (**G**) Cell apoptosis of tumors were detected by TUNEL staining.

https://doi.org/10.2147/IJN.S384196 DovePress

Histology Analysis

Tumor, organ and skin tissues were collected immediately after the mice were sacrificed, and then fixed with 10% neutral buffer formalin for 24 h, prepared into paraffin, sectioned and stained with hematoxylin and eosin (H&E), finally were examined by digital microscope.

Results and Discussion

Preparation and Characterization of PyTPA@PEG and TB@PEG NPs

According to our previous report, we synthesized the AIE-photosensitizer PyTPA (Figure S1A) and PTPA-BDTO (TB) (Figure S2A).[60,61] UV-vis characteristic absorption spectra of PyTPA and TB were shown in Figure S1B and S2B. PyTPA and TB had two characteristic absorption peaks at 445 nm and 530 nm, which was one of the most critical reasons for choosing the two photosensitizers. The fluorescence of PyTPA (Figure S1C) and TB (Figure S2C) could reach the near infrared range (~680 nm). With the increase of the water fractions, PyTPA and TB gradually aggregated and their fluorescence increased (Figure S1D, S1E, S2D and S2E), indicating that PyTPA and TB were AIEgens.[62–64] Since PyTPA and TB are hardly soluble in aqueous medium, to increase water dispersibility as well as biocompatibility, PyTPA and TB are processed into nanoparticles (NPs) by using biocompatible encapsulation matrix of 1.2-distearoyl-sn-glycero-3-phosphoethanolamine-N [methoxy (polyethylene glycol)-2000] (PEG-DSPE 2000) through common nanoprecipitation method.[65–68] Because DSPE-PEG2000 has no obvious UV absorption and fluorescence (Figure S3), the obtained PyTPA@PEG and TB@PEG NPs showed similar UV/Vis absorption and fluorescence spectra as that of PyTPA and TB (Figure 2A, D). PyTPA@PEG and TB@PEG could be well dispersed in aqueous environment with a hydrodynamic diameter of 125.9 nm (PDI = 0.096) and 157.7 nm (PDI = 0.154), as measured by dynamic light scattering (DLS) (Figure 2B and E). The ζ-potential of PyTPA@PEG was −25.1 mV, and that of TB@PEG was −36.9 mV (Figure S4). Transmission electron microscopy (TEM) image confirmed the sphere morphology and particle size of PyTPA@PEG and TB@PEG (Figure 2C and F). Compared with the DLS result, the similar to the mean particle size observed from the TEM image, which is conducive to the accumulation of NPs in tumor tissues via the enhanced permeability and retention (EPR) effect.[69] Importantly, the PyTPA@PEG and TB@PEG in PBS solution without markedly changing the specific particle size values of NPs within 7 days at room temperature (Figure 2G), suggesting that NPs enjoy great colloidal stability.

Noteworthy, the PyTPA@PEG and TB@PEG NPs can also produce ROS during light exposure, as indicated by indicator ABDA, whose absorption decreased at 378 nm by the reaction with ROS (Figure S5 and S6). Under the same experimental conditions, comparing with the TB@PEG NPs, PyTPA@PEG possessed is better photosensitivity than TB@PEG. As pointed in Figure 2H and I, the ROS can be produced by nanoparticles at the same concentration upon white light, a 532 nm laser and white light from penetrating skin of mice, all at an intensity of 80 mW cm^{-2}. More interestingly, for both PyTPA@PEG and TB@PEG, the absorption decreased at 378 nm of ABDA is rapidly increased under white light irradiation, while the 532 nm laser and white light penetrating the skin groups show more slowly, suggesting that white light is more universal and more effective than laser for photosensitizers. Since PyTPA@PEG had a small absorption value at 532 nm and a maximum absorption value of around 440 nm, the 532 nm laser wavelength did not effectively encourage the production of ROS by PyTPA@PEG NPs. Although 532 nm was the optimum excitation wavelength for TB@PEG, most of TB@PEG's absorption wavelength could also be covered by the wavelength range of white light, which even included the optimum excitation wavelength. Thus, compared with laser, white light may have a major benefit over laser in activating PSs to produce ROS. White light covers almost the whole wavelength region of visible light and can completely meet all absorption peaks of photosensitive in the range of visible light, which may be the main reason for its high efficiency of PDT as an excitation source.[70] At the same time, it also shows that white light does not penetrate the skin easily. After irradiating PyTPA@PEG solution with 80 mW white light for 5 minutes, ABDA UV absorption of the white light group decreased by 97.5%, while that of the laser group only decreased by 44.8%, and white light penetration of skin decreased by 20.4%. After irradiating TB@PEG solution for 20 minutes, the decrease trend was similar to that of PyTPA@PEG: 88.2% in the white light group, 60.3% in the laser group and only 41.0% in the white light penetrating the skin. The results indicated that white light have successfully and efficiently induced the ROS from nanoparticles, which had universal applicability to

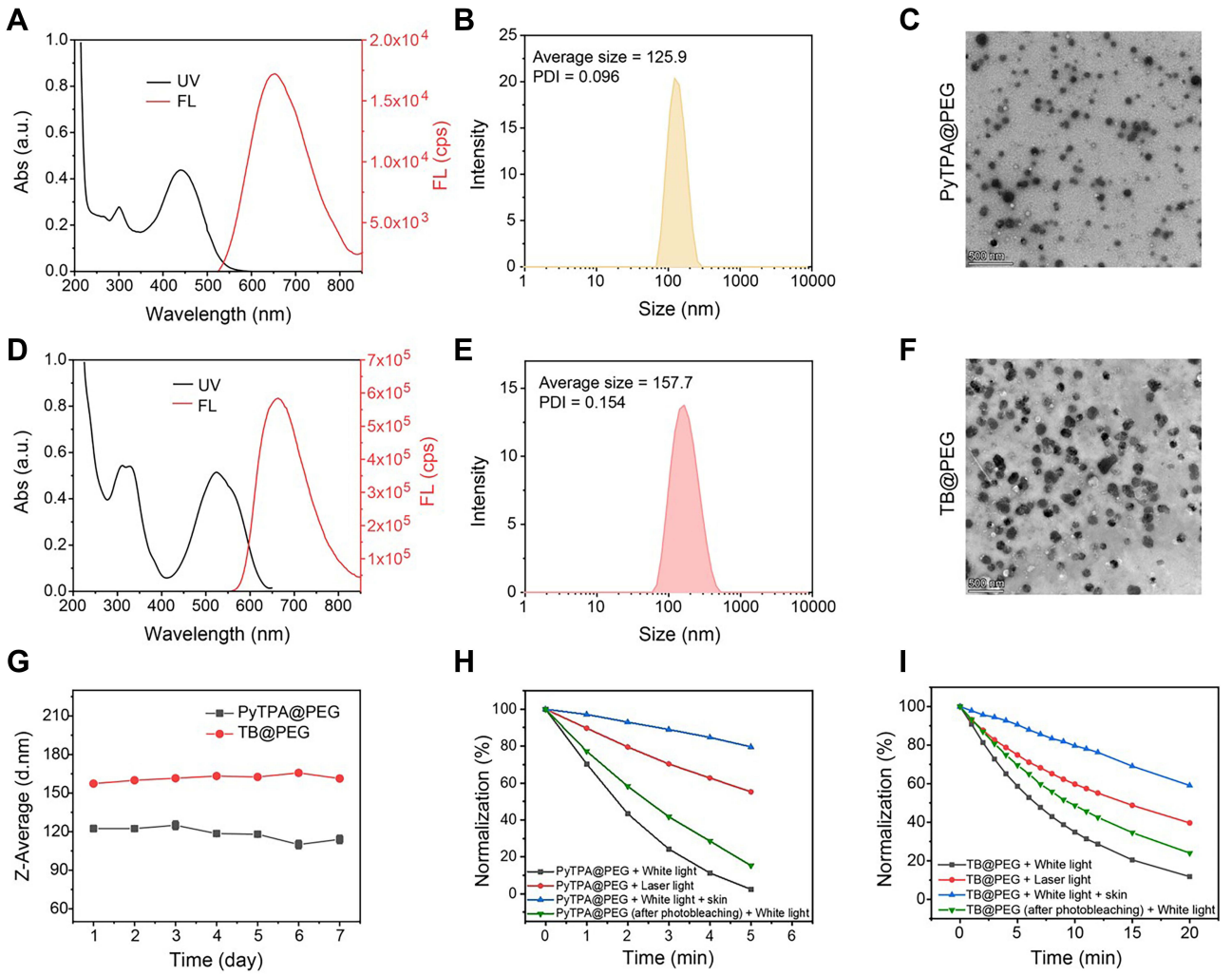

Figure 2 Characterization of PyTPA@PEG and TB@PEG NPs. (**A**) UV-vis absorption and fluorescence spectra of PyTPA@PEG. The concentration of PyTPA@PEG is 10 μM (Ex = 450 nm). (**B**) Hydrodynamic size distribution of PyTPA@PEG. (**C**) TEM image of PyTPA@PEG. Scale bar: 500 nm. (**D**) UV-vis absorption and fluorescence spectra of TB@PEG. The concentration of TB@PEG is 10 μM (Ex = 530 nm). (**E**) Hydrodynamic size distribution of TB@PEG. (**F**) TEM image of PyTPA@PEG. Scale bar: 500 nm. (**G**) Stability assay of PyTPA@PEG and TB@PEG NPs in PBS solution at room temperature. (**H**) Photosensitivity of PyTPA@PEG upon light irradiation (white light, 80 mW cm^{-2}, 532 nm laser light, 80 mW cm^{-2}). The concentration of PyTPA@PEG is 5 μM. (**I**) Photosensitivity of TB@PEG upon light irradiation (white light, 80 mW cm^{-2}, 532 nm laser light, 80 mW cm^{-2}). The concentration of TB@PEG is 5 μM.

photosensitizer, and the photodynamic effect was obviously better than that of laser. But it also showed that the problem of poor white light penetration needs to be solved. In addition, the ROS-production capacity of the photosensitizer PyTPA@PEG after photobleaching does not significantly reduce, only about 12%, and its ROS production effect was still excellent. At the same time, the anti-photobleaching performance of TB@PEG has the same is almost as good as that of PyTPA@PEG. Compared with AIE PSs, the ROS production capacity of RB decreased significantly after photobleaching, reaching about 25% (Figure S7). The results confirm that PyTPA@PEG and TB@PEG exhibit excellent photobleaching resistance, stability and light-induced ROS-generation capability.

PyTPA@PEG and TB@PEG NPs-Mediated PDT Killed Tumor Cells

To study the cellular uptake of PyTPA@PEG and TB@PEG NPs, cellular imaging is carried out by fluorescence microscopy. PyTPA@PEG NPs were incubated with Hela cells for 4 h, strong red fluorescence signal can be successfully detected in HeLa cells under 488 nm excitation (Figure S8). And fluorescence signal can be observed after cultured with TB@PEG NPs for 24 h under 488 nm excitation (Figure S9). Next, we investigated the photodynamic effect of PyTPA@PEG and TB@PEG NPs by three kinds of light source in vitro, including white light, 532 nm laser and

white light penetrating the skin. As shown in Figure 3A, Hela cells cultured by PyTPA@PEG NPs were incubated with 2.7-dichlorodihydrofluorescein diacetate (DCFH-DA), which has been used for detecting several ROS in biological media. After irradiation with light, green fluorescence (DCFH-DA) was observed in white light, 532 nm laser irradiation

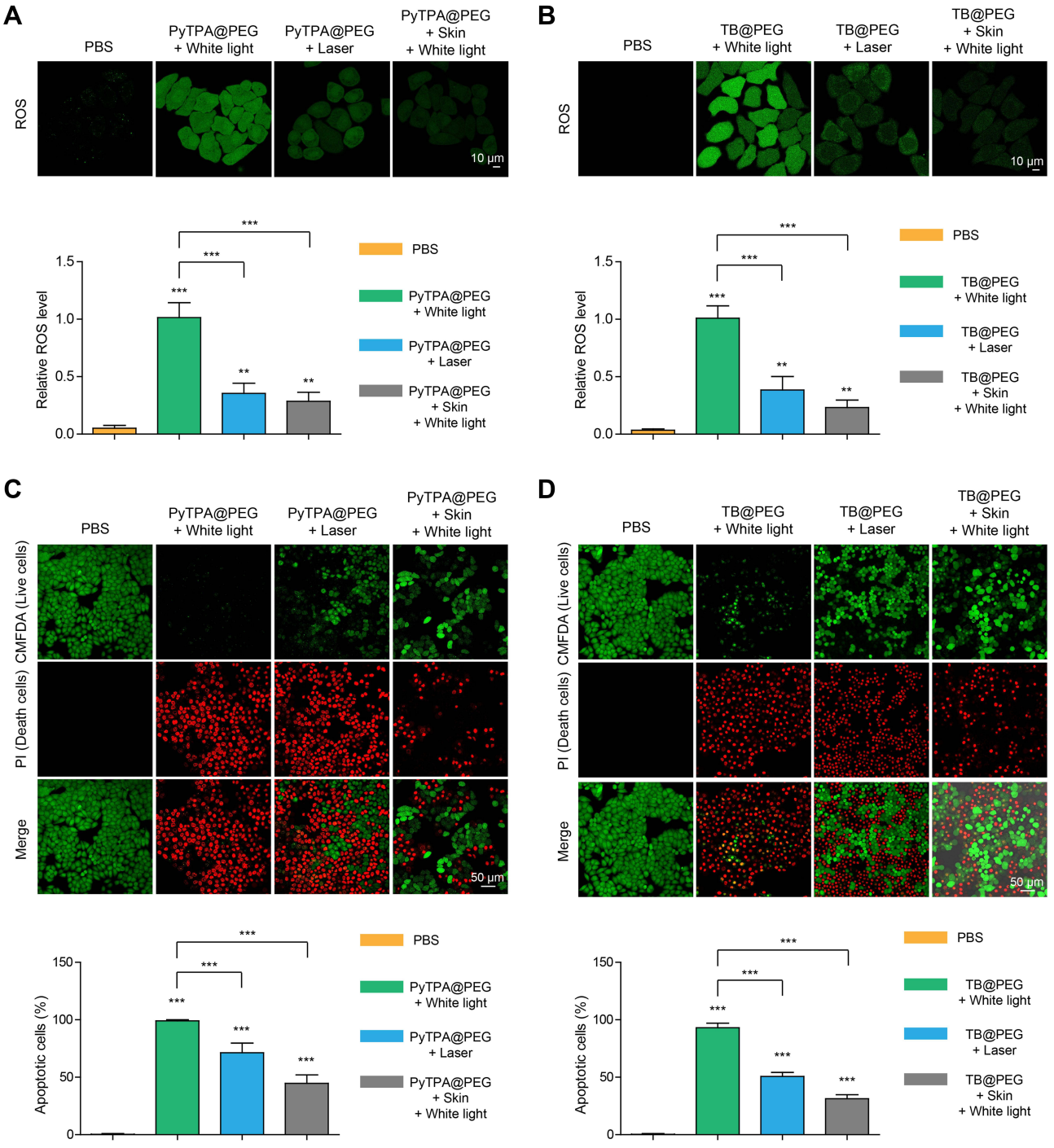

Figure 3 In vitro cell experiments. (**A**) Detection of intracellular ROS generation by DCFH-DA in HeLa cells after incubation with PyTPA@PEG NPs (10 μM), followed by white light, 532 nm laser irradiation and white light penetration of skin (all light intensity: 200 mW cm^{-2}, time: 3min). (**B**) Detection of intracellular ROS generation after incubation with TB@PEG NPs (10 μM), followed by light (all light intensity: 200 mW cm^{-2}, time: 5 min). (**C**) Hela cells were cultured with PyTPA@PEG NPs (20 μM) and then irradiated with white light, 532 nm laser irradiation and white light penetration of skin (all light intensity: 200 mW cm^{-2}, time: 3 min). CMFDA: Ex = 488 nm; Em = 540 nm. PI: Ex = 543 nm; Em = 650 nm. (**D**) Hela cells were incubated with TB@PEG NPs (30 μM) and treatment with different light irradiation (all light intensity: 200 mW cm^{-2}, time: 5 min). Data are represented as mean ± standard deviation (SD) and analyzed by two-sided Student's *t*-test. **p < 0.01, ***p < 0.001.
Abbreviation: n.s., not significant.

and white light penetration of skin groups, which indicated that PyTPA@PEG NPs could produce ROS under light irradiation. The fluorescence intensity of the white light group was the strongest, followed by the 532 nm laser group, while that of the skin group was the weakest. The results showed that white light can induce photosensitizers to produce ROS efficiently, but the penetration depth is greatly deficient. The experimental results of TB@PEG NPs, like PyTPA@PEG NPs, explained the problem of white light penetration depth (Figure 3B). Furthermore, the viability of the Hela cells was evaluated using 5-chloromethyl fluorescein diacetate (CMFDA) and propidium iodide (PI) after cultured with PyTPA@PEG and TB@PEG NPs upon white light, 532 nm laser and white light penetration of skin irradiation (Figure 3C and D). Hela cells in the white light group were almost all dead, indicating that AIE photosensitizer has excellent killing effect. Moreover, the numbers of the death cells in white light groups were more than that in 532 nm laser, suggesting that the maximum PDT effect was produced in the white light group and significantly better than the laser group. However, the number of dead cells in the group with white light penetration of skin was the least compared with the white light group and the laser group, indicating that white light had a weak ability to penetrate the skin, which ultimately led to the reduction of PDT effect. Therefore, it is urgent to find a solution to overcome this shortcoming, so as to facilitate the better application of white light.

Circulation Kinetics and Biodistribution of Nanoparticles in vivo

Hemolysis test was performed to evaluate the blood compatibility of PyTPA@PEG and TB@PEG NPs.[71,72] As shown in Figure 4A, after incubated with phosphate-buffered saline (PBS, negative control), PyTPA@PEG, TB@PEG, and ultrapure water (positive control), negligible hemolysis happened in the two nanoparticle groups as well as the PBS. However, a significant amount of hemoglobin was observed in the ultrapure water. By UV/Vis absorption analysis of the solution, it was determined that the hemolysis ratio of PyTPA@PEG and TB@PEG groups was lower than 5% at various concentrations even at a concentration of 30 μM, so there was permissible to inject nanoparticles into the tail vein of mice (Figure S10). Next, HeLa tumor-bearing mice were established and the tumor imaging effect of TB@PEG NPs in vivo was investigated to determine the optimal time for phototherapy. It was known that excellent circulation of drugs in the body was conducive to the enrichment of nanoparticles in tumors. The fluorescence in blood becomes reduced gradually in a time-dependent manner after injection of PyTPA@PEG NPs into tumor-bearing mice via the tail vein (Figure 4B). Similarly, TB@PEG NPs exhibited excellent circularity in vivo, as shown in Figure 4C. It showed that PyTPA@PEG NPs and TB@PEG NPs were characterized by prolongation of circulation in vivo that allowed them to passively target tumors by enhancing EPR effect. In vivo imaging at various intervals revealed that fluorescence in the tumor grew progressively over time, with the fluorescence intensity remained high at 48 hours (Figure 4D and E). Thereafter, in the case of TB@PEG, tumor and organs (heart, liver, spleen, lung and kidneys) were resected from the tumor-bearing mice at 48 h post-injection for fluorescence imaging to study the NPs distribution. As shown in Figure S11A, strong fluorescence was observed in the tumor tissue and liver, followed by the spleen, and almost no fluorescence was observed for heart, lung and kidney in terms of the intensity of fluorescence signal. Figure S11B showed the relative fluorescence intensity of tumors and organs measured by a semi-quantitative biodistribution analysis. These results suggested that NPs could accumulate well in tumor tissue, which provided a prerequisite for local photodynamic therapy of tumors.

Using Optical Fiber to Deliver White Light for PDT in vivo

Since white light is blocked by the skin, the effect of PDT is less satisfactory. Therefore, it is particularly important to use optical fiber delivery white light for intratumor light therapy in mice. In order to evaluate the in vivo antitumor efficacy of the white light delivering to tumors via optical fiber, we used a HeLa tumor-bearing mice model for this experiment. The schematic illustration of tumor model construction and treatment process are shown in Figure 1A. Figure 1B illustrates how optical fiber is used, including extratumoral light irradiation (E-L) and intratumoral light irradiation (I-L). The mice are divided into five groups were i.v. injected with PBS, PyTPA@PEG and TB@PEG NPs. Twenty mice were divided into five groups: PBS, TB@PEG (E-L), PyTPA@PEG (E-L), TB@PEG (I-L), and PyTPA@PEG (I-L). In PBS group, the tumor grows rapidly as the time elapsed. The growth of the tumors in TB@PEG (E-L), PyTPA@PEG (E-L), TB@PEG (I-L), and PyTPA@PEG (I-L) groups was significantly inhibited compared with PBS group (Figure 1C and D). This suggested that

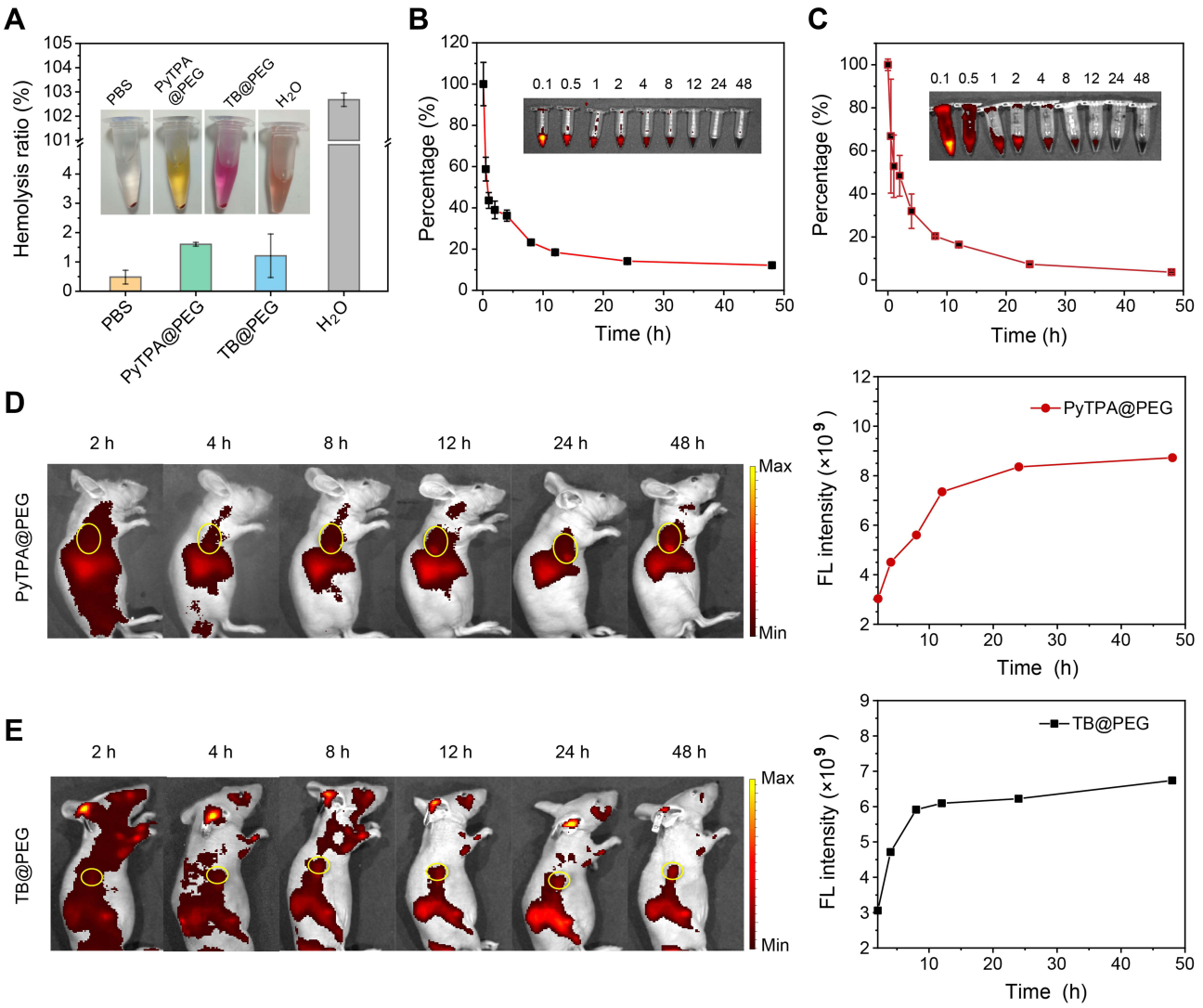

Figure 4 Circulation kinetics and bio-distribution of NPs. (**A**) Hemolysis test after incubated with PBS (negative control), PyTPA@PEG, TB@PEG, and ultrapure water (positive control). The results were presented as the mean ±SD (n = 3). (**B**) and (**C**) Relative fluorescence intensity of PyTPA@PEG (0.5 mg mL^{-1}, 100 μL) and TB@PEG (0.5 mg mL^{-1}, 100 μL) in the blood after injection via the tail vein and circulation profile in mice. The results were presented as the mean ± SD (n = 3). (**D**) and (**E**) Fluorescence images in vivo and fluorescence intensity of tumor of PyTPA@PEG and TB@PEG with different injection time after the tail vein injection. PyTPA @PEG: Ex = 465 nm, Em = 660 nm. TB@PEG: Ex = 535 nm, Em = 680 nm.

white light could induce PDT of most photosensitizers, which lead to increased apoptosis/necrosis of tumor cells. Noteworthy, both TB@PEG (I-L) and PyTPA@PEG (I-L) groups inhibited tumor growth better than TB@PEG (E-L) and PyTPA@PEG (E-L) groups. According to the results illustrated that tumor growth could be significantly inhibited when improved the effect of PDT by delivering white light into the tumor by optical fiber to increase the penetration depth of light. Additionally, as shown in Figure 1E, there was no significant weight loss for all groups of mice. Hematoxylin and eosin (H&E) assays were used to analyze the organs in PBS, PyTPA@PEG (E-L) and PyTPA@PEG (I-L) groups after administration. As shown in Figure S12, H&E staining revealed that the heart, liver, lung, spleen, and kidney in each group was no detectable phenomenon of inflammation or tissue damage, indicating that the toxicity of NPs is very weak. At the same time, H&E staining revealed that tumor tissues in PBS group were compact, whereas tumors in PyTPA@PEG (E-L) and PyTPA@PEG (I-L) groups were sparse (Figure 1F). Especially in PyTPA@PEG (I-L) group, more necrotic tumor cells could be found than PyTPA@PEG (E-L) group. As shown in Figure 1G, TUNEL staining exhibited almost no apoptosis in PBS group, few apoptotic cells in PyTPA@PEG (E-L) group, and abundant apoptotic tumor cells in PyTPA@PEG (I-L) group. These results abundantly indicated that interstitial light delivery using fiber was beneficial for the treatment of deep-

seated tumours, improving PDT efficiency and increasing the apoptosis of tumor cells. Meanwhile, after white light irradiation, skin H&E staining 24 hours later showed dense tissue, with no significant difference from that of the control group, while obvious tissue sparseness was observed in the laser irradiation group. The black arrow in Figure S13 indicated inflammatory cell infiltration, which further confirmed the safety performance of white light.

Conclusion

In this work, we synthesized two AIE molecules with photosensitive properties, named PyTPA and TB respectively. By encapsulating them within polymeric matrix (PEG-DSPE 2000), the prepared versatile PyTPA@PEG and TB@PEG NPs were formulated for tumor imaging and therapy. Our solution study showed that although the excitation wavelength of PyTPA@PEG NPs was 440 nm and that of TB@PEG NPs was 524 nm, they both hold high stability, strong near-infrared fluorescence (~680 nm), excellent photobleaching resistance and effective ROS generation. Especially under the irradiation of white light, ROS generation of nanoparticles was significantly better than that of laser. However, ROS production of nanoparticles was lowest when white light penetrated the skin. Detection of intracellular ROS generation in cells and the viability tests also revealed the same results. In order to solve the problem of insufficient penetration of white light, the white optical fiber-mediated photodynamic therapy was used to destroy the tumor by irradiating the interior of the tumor. In vivo experiments strongly announced that interventional fiber-optic therapy significantly improved the therapeutic efficacy of tumor. The advantages of white light interventional fiber-optic therapy, such as versatility for most photosensitizers, high safety in use, easy management of postoperative instruments and excellent efficiency of ROS generation, especially for photodynamic therapy deep into the tumor could be further combined with other clinical photosensitizers and therapeutic techniques to achieve safer and more effective clinical application.

Acknowledgments

This work is supported by the National Natural Science Foundation of China (22090050, 22104040, 21974128 and 21874121), the Natural Science Foundation of Hubei Province (2020CFA037).

Disclosure

The authors report no conflicts of interest in this work.

References

1. Sung H, Ferlay J, Siegel RL., et al. Global cancer statistics 2020: globocan estimates of incidence and mortality worldwide for 36 cancers in 185 countries. *CA Cancer J Clin*. 2021;71(3):209–249. doi:10.3322/caac.21660
2. Bray F, Laversanne M, Weiderpass E, Soerjomataram I. The ever-increasing importance of cancer as a leading cause of premature death worldwide. *Cancer*. 2021;127(16):3029–3030. doi:10.1002/cncr.33587
3. Dougherty TJ, Gomer CJ, Henderson BW, et al. Photodynamic Therapy. *JNCI-J Natl Cancer I*. 1998;90(12):889–905. doi:10.1093/jnci/90.12.889
4. Dai J, Cheng Y, Wu J, et al. Modular peptide probe for pre/intra/postoperative therapeutic to reduce recurrence in ovarian cancer. *ACS Nano*. 2020;14(11):14698–14714. doi:10.1021/acsnano.9b09818
5. Jia D, Ma X, Lu Y, et al. ROS-responsive cyclodextrin nanoplatform for combined photodynamic therapy and chemotherapy of cancer. *Chin Chem Lett*. 2021;32(1):162–167. doi:10.1016/j.cclet.2020.11.052
6. Dai J, Hu JJ, Dong X, et al. Deep downregulation of PD-L1 by caged peptide-conjugated AIEgen/miR-140 nanoparticles for enhanced immunotherapy. *Angew Chem Int Ed*. 2022:e202117798. doi:10.1002/anie.202117798
7. Cui D, Li J, Zhao X, Pu K, Zhang R. Semiconducting polymer nanoreporters for near-infrared chemiluminescence imaging of immunoactivation. *Adv Mater*. 2020;32(6):1906314. doi:10.1002/adma.201906314
8. Zeng Z, Zhang C, Li J, Cui D, Jiang Y, Pu K. Activatable polymer nanoenzymes for photodynamic immunometabolic cancer therapy. *Adv Mater*. 2021;33(4):2007247. doi:10.1002/adma.202007247
9. Zhuang Z, Dai J, Yu M, et al. Type I photosensitizers based on phosphindole oxide for photodynamic therapy: apoptosis and autophagy induced by endoplasmic reticulum stress. *Chem Sci*. 2020;11(13):3405–3417. doi:10.1039/d0sc00785d
10. Meng Z, Xue H, Wang T, et al. Aggregation-induced emission photosensitizer-based photodynamic therapy in cancer: from chemical to clinical. *J Nanobiotechnol*. 2022;20(1):344. doi:10.1186/s12951-022-01553-z
11. Long Z, Hu -J-J, Yuan L, et al. A cell membrane-anchored nanoassembly with self-reporting property for enhanced second near-infrared photothermal therapy. *Nano Today*. 2021;41:101312. doi:10.1016/j.nantod.2021.101312
12. Lopez RFV, Lange N, Guy R, Bentley MVLB. Photodynamic therapy of skin cancer: controlled drug delivery of 5-ALA and its esters. *Adv Drug Delivery Rev*. 2004;56(1):77–94. doi:10.1016/j.addr.2003.09.002

13. Morton CA, Szeimies RM, Basset-Seguin N, Calzavara-Pinton P, Gilaberte Y. European dermatology forum guidelines on topical photodynamic therapy 2019 part 1: treatment delivery and established indications-actinic keratoses, Bowen's disease and basal cell carcinomas. *J Eur Acad Dermatol Venereol*. 2019;33(12):2225–2238. doi:10.1111/jdv.16017
14. Li X, Lovell JF, Yoon J, Chen X. Clinical development and potential of photothermal and photodynamic therapies for cancer. *Nat Rev Clin Oncol*. 2020;17(11):657–674. doi:10.1038/s41571-020-0410-2
15. Zhang L, Ding D. Recent advances of transition Ir(III) complexes as photosensitizers for improved photodynamic therapy. *View*. 2021;2 (6):20200179. doi:10.1002/VIW.20200179
16. Jiang N, Zhou Z, Xiong W, et al. Tumor microenvironment triggered local oxygen generation and photosensitizer release from manganese dioxide mineralized albumin-ICG nanocomplex to amplify photodynamic immunotherapy efficacy. *Chin Chem Lett*. 2021;32(12):3948–3953. doi:10.1016/j.cclet.2021.06.053
17. Shen L, Zhou T, Fan Y, et al. Recent progress in tumor photodynamic immunotherapy. *Chin Chem Lett*. 2020;31(7):1709–1716. doi:10.1016/j.cclet.2020.02.007
18. Liu Z, Zou H, Zhao Z, et al. Tuning organelle specificity and photodynamic therapy efficiency by molecular function design. *ACS Nano*. 2019;13 (10):11283–11293. doi:10.1021/acsnano.9b04430
19. Hu F, Xu S, Liu B. Photosensitizers with aggregation-induced emission: materials and biomedical applications. *Adv Mater*. 2018;30(45):1801350. doi:10.1002/adma.201801350
20. Guo J, Dai J, Peng X, et al. 9,10-Phenanthrenequinone: a promising kernel to develop multifunctional antitumor systems for efficient type I photodynamic and photothermal synergistic therapy. *ACS Nano*. 2021;15(12):20042–20055. doi:10.1021/acsnano.1c07730
21. Cheng Y, Dai J, Sun C, et al. An intracellular H_2O_2-responsive AIEgen for the peroxidase-mediated selective imaging and inhibition of inflammatory cells. *Angew Chem Int Ed*. 2018;57(12):3123–3127. doi:10.1002/anie.201712803
22. Chen K, Zhang R, Wang Z, Zhang W, Tang BZ. Structural modification orientated multifunctional AIE fluorescence probes: organelles imaging and effective photosensitizer for photodynamic therapy. *Adv Opt Mater*. 2019;8(2):1901433. doi:10.1002/adom.201901433
23. Bu F, Duan R, Xie Y, et al. Unusual aggregation-induced emission of a coumarin derivative as a result of the restriction of an intramolecular twisting motion. *Angew Chem Int Ed*. 2015;54(48):14492–14497. doi:10.1002/anie.201506782
24. Wan Q, Zhang R, Zhuang Z, et al. Molecular engineering to boost AIE-active free radical photogenerators and enable high-performance photodynamic therapy under hypoxia. *Adv Funct Mater*. 2020;30(39):2002057. doi:10.1002/adfm.202002057
25. Ni J-S, Min T, Li Y, et al. Planar AIEgens with enhanced solid-state luminescence and ROS generation for multidrug-resistant bacteria treatment. *Angew Chem Int Ed*. 2020;59(25):10179–10185. doi:10.1002/anie.202001103
26. Dai J, Wu X, Ding S, et al. Aggregation-induced emission photosensitizers: from molecular design to photodynamic therapy. *J Med Chem*. 2020;63 (5):1996–2012. doi:10.1021/acs.jmedchem.9b02014
27. Luo JD, Xie ZL, Lam JWY, et al. Aggregation-induced emission of 1-methyl-1,2,3,4,5-pentaphenylsilole. *Chem Commun*. 2001:1740–1741. doi:10.1039/b105159h
28. Gao M, Tang BZ. Aggregation-induced emission probes for cancer theranostics. *Drug Discov Today*. 2017;22(9):1288–1294. doi:10.1016/j.drudis.2017.07.004
29. Zhou T, Hu R, Wang L, et al. An AIE-active conjugated polymer with high ROS-generation ability and biocompatibility for efficient photodynamic therapy of bacterial infections. *Angew Chem Int Ed*. 2020;59(25):9952–9956. doi:10.1002/anie.201916704
30. Dai J, Li Y, Long Z, et al. Efficient near-infrared photosensitizer with aggregation-induced emission for imaging-guided photodynamic therapy in multiple xenograft tumor models. *ACS Nano*. 2020;14(1):854–866. doi:10.1021/acsnano.9b07972
31. Li Y, Zhang RY, Wan Q, et al. Trojan horse-like nano-AIE aggregates based on homologous targeting strategy and their photodynamic therapy in anticancer application. *Adv Sci*. 2021;8(23):2102561. doi:10.1002/advs.202102561
32. Li H, Zhu W, Li M, et al. Side area-assisted 3D evaporator with antibiofouling function for ultra-efficient solar steam generation. *Adv Mater*. 2021;33(36):2102258. doi:10.1002/adma.202102258
33. Wu W, Xu S, Qi G, et al. A cross-linked conjugated polymer photosensitizer enables efficient sunlight-induced photooxidation. *Angew Chem Int Ed*. 2019;58(10):3062–3066. doi:10.1002/anie.201811067
34. Yuan G, Lv C, Liang J, et al. Molecular engineering of efficient singlet oxygen generators with near-infrared AIE features for mitochondrial targeted photodynamic therapy. *Adv Funct Mater*. 2021;31(36):2104026. doi:10.1002/adfm.202104026
35. Wu M, Liu X, Chen H, et al. Activation of pyroptosis by membrane-anchoring AIE photosensitizer design: new prospect for photodynamic cancer cell ablation. *Angew Chem Int Ed*. 2021;60(16):9093–9098. doi:10.1002/anie.202016399
36. Zhuang Z, Meng Z, Li J, et al. Antibacterial theranostic agents with negligible living cell invasiveness: AIE-active cationic amphiphiles regulated by alkyl chain engineering. *ACS Nano*. 2022;16(8):11912–11930. doi:10.1021/acsnano.2c01721
37. Li J, Meng Z, Zhuang Z, et al. Effective Therapy of drug-resistant bacterial infection by killing planktonic bacteria and destructing biofilms with cationic photosensitizer based on phosphindole oxide. *Small*. 2022;18(17):2200743. doi:10.1002/smll.202200743
38. Dai J, Wu M, Wang Q, et al. Red blood cell membrane-camouflaged nanoparticles loaded with AIEgen and Poly(I:C) for enhanced tumoral photodynamic-immunotherapy. *Natl Sci Rev*. 2021;8(6):nwab039. doi:10.1093/nsr/nwab039
39. Li J, Wang J, Li H, Song N, Wang D, Tang BZ. Supramolecular materials based on AIE luminogens (AIEgens): construction and applications. *Chem Soc Rev*. 2020;49(4):1144–1172. doi:10.1039/C9CS00495E
40. Li W, Zhang Y, Wang Y, et al. Nucleic acids induced peptide-based AIE nanoparticles for fast cell imaging. *Chin Chem Lett*. 2021;32 (4):1571–1574. doi:10.1016/j.cclet.2020.09.054
41. Liu S, Li Y, Kwok RTK, Lam JWY, Tang BZ. Structural and process controls of AIEgens for NIR-II theranostics. *Chem Sci*. 2021;12 (10):3427–3436. doi:10.1039/D0SC02911D
42. Zhang J, He B, Hu Y, et al. Stimuli-responsive AIEgens. *Adv Mater*. 2021;33(32):2008071. doi:10.1002/adma.202008071
43. Xu W, Wang D, Tang BZ. NIR-II AIEgens: a win–win integration towards bioapplications. *Angew Chem Int Ed*. 2021;60(14):7476–7487. doi:10.1002/anie.202005899
44. Wu X, Wu J, Dai J, et al. Aggregation-induced emission luminogens reveal cell cycle-dependent telomerase activity in cancer cells. *Natl Sci Rev*. 2021;8(6):nwaa306. doi:10.1093/nsr/nwaa306

45. Hu -J-J, Dong X, Jiang W, Xia F, Lou X. Multifunctional aggregates for precise cellular analysis. *Sci China Chem*. 2021;64(11):1938–1945. doi:10.1007/s11426-021-1051-9
46. Yang J, Hu -J-J, Wei J, et al. Peptide-conjugated aggregation-induced emission fluorogen: precise and firm cell membrane labeling by multiple weak interactions. *CCS Chem*. 2021;4(2):464–475. doi:10.31635/ccschem.021.202101349
47. Goldman L. A review: applications of the laser beam in cancer biology. *Int J Cancer*. 1966;1(4):309–318. doi:10.1002/ijc.2910010402
48. Sultan RA. Tumour ablation by laser in general surgery. *Lasers Med Sci*. 1990;5(2):185–193. doi:10.1007/BF02031380
49. Wang B, Shi L, Zhang YF, et al. Gain with no pain? Pain management in dermatological photodynamic therapy. *Br J Dermatol*. 2017;177(3):656–665. doi:10.1111/bjd.15344
50. Wiegell SR, Hædersdal M, Philipsen PA, Eriksen P, Enk CD, Wulf HC. Continuous activation of PpIX by daylight is as effective as and less painful than conventional photodynamic therapy for actinic keratoses; a randomized, controlled, single-blinded study. *Br J Dermatol*. 2008;158(4):740–746. doi:10.1111/j.1365-2133.2008.08450.x
51. Wu X, Xu M, Wang S, et al. F,N-doped carbon dots as efficient type I photosensitizers for photodynamic therapy. *Dalton Trans*. 2022;51(6):2296–2303. doi:10.1039/D1DT03788A
52. Wang J, Xu M, Wang D, et al. Copper-doped carbon dots for optical bioimaging and photodynamic therapy. *Inorg Chem*. 2019;58(19):13394–13402. doi:10.1021/acs.inorgchem.9b02283
53. Wang S, Ma M, Liang Q, et al. Single-atom manganese anchored on carbon dots for promoting mitochondrial targeting and photodynamic effect in cancer treatment. *ACS Appl Nano Mater*. 2022;5(5):6679–6690. doi:10.1021/acsanm.2c00716
54. Li Z, Wang D, Xu M, et al. Fluorine-containing graphene quantum dots with a high singlet oxygen generation applied for photodynamic therapy. *J Mater Chem B*. 2020;8(13):2598–2606. doi:10.1039/C9TB02529D
55. Hu X, Wang S, Luo Q, et al. Synthesis of Sn nanocluster@carbon dots for photodynamic therapy application. *Chin Chem Lett*. 2021;32(7):2287–2291. doi:10.1016/j.cclet.2021.01.039
56. Yamamoto M, Shitomi K, Miyata S, Miyaji H, Aota H, Kawasaki H. Bovine serum albumin-capped gold nanoclusters conjugating with methylene blue for efficient $^1O_2$ generation via energy transfer. *J Colloid Interface Sci*. 2018;510:221–227. doi:10.1016/j.jcis.2017.09.011
57. Fan W, Huang P, Chen X. Overcoming the Achilles' heel of photodynamic therapy. *Chem Soc Rev*. 2016;45(23):6488–6519. doi:10.1039/c6cs00616g
58. Ochsner M. Light scattering of human skin: a comparison between zinc(II)— phthalocyanine and photofrin II. *J Photochem Photobiol B*. 1996;32(1):3–9. doi:10.1016/1011-1344(95)
59. Liu Y, Meng X, Bu W. Upconversion-based photodynamic cancer therapy. *Coord Chem Rev*. 2019;379:82–98. doi:10.1016/j.ccr.2017.09.006
60. Yang J, Dai J, Wang Q, et al. Tumor-triggered disassembly of a multiple-agent-therapy probe for efficient cellular internalization. *Angew Chem Int Ed*. 2020;59(46):20405–20410. doi:10.1002/anie.202009196
61. Zhen S, Wang S, Li S, et al. Theranostics: efficient red/near-infrared fluorophores based on benzo[1,2-b:4,5-b′]dithiophene 1,1,5,5-tetraoxide for targeted photodynamic therapy and *in vivo* two-photon fluorescence bioimaging. *Adv Funct Mater*. 2018;28(13):1870087. doi:10.1002/adfm.201870087
62. Gu B, Wu WB, Xu GX, et al. Precise two-photon photodynamic therapy using an efficient photosensitizer with aggregation-induced emission characteristics. *Adv Mater*. 2017;29:28. doi:10.1002/adma.201701076
63. Che W, Zhang L, Li Y, et al. Ultrafast and noninvasive long-term bioimaging with highly stable red aggregation-induced emission nanoparticles. *Anal Chem*. 2019;91(5):3467–3474. doi:10.1021/acs.analchem.8b05024
64. Xia Q, Chen Z, Yu Z, Wang L, Qu J, Liu R. Aggregation-induced emission-active near-infrared fluorescent organic nanoparticles for noninvasive long-term monitoring of tumor growth. *ACS Appl Mater Interfaces*. 2018;10(20):17081–17088. doi:10.1021/acsami.8b03861
65. Dai J, Dong X, Wang Q, Lou X, Xia F, Wang S. PEG-polymer encapsulated aggregation-induced emission nanoparticles for tumor theranostics. *Adv Healthc Mater*. 2021;10(24):2101036. doi:10.1002/adhm.202101036
66. Jiang R, Dai J, Dong X, et al. Improving image-guided surgical and immunological tumor treatment efficacy by photothermal and photodynamic therapies based on a multifunctional NIR AIEgen. *Adv Mater*. 2021;33(22):2101158. doi:10.1002/adma.202101158
67. Zhang L, Li Y, Che W, et al. AIE multinuclear Ir(III) complexes for biocompatible organic nanoparticles with highly enhanced photodynamic. *Adv Sci*. 2019;6(5):1802050. doi:10.1002/advs.201802050
68. Qian YX, Wang YH, Jia F, et al. Tumor-microenvironment controlled nanomicelles with AIE property for boosting cancer therapy and apoptosis monitoring. *Biomaterials*. 2019;188:96–106. doi:10.1016/j.biomaterials.2018.10.003
69. Cui L, Lin Q, Jin CS, et al. A PEGylation-free biomimetic porphyrin nanoplatform for personalized cancer theranostics. *ACS Nano*. 2015;9(4):4484–4495. doi:10.1021/acsnano.5b01077
70. Mordon S, Maunoury V. Using white light during photodynamic therapy: visualization only or treatment? *Eur J Gastroenterol Hepatol*. 2006;18(7):765–771. doi:10.1097/01.meg.0000223910.08611.79
71. Yi X, Hu -J-J, Dai J, et al. Self-guiding polymeric prodrug micelles with two aggregation-induced emission photosensitizers for enhanced chemo-photodynamic therapy. *ACS Nano*. 2021;15(2):3026–3037. doi:10.1021/acsnano.0c09407
72. Gunsolus IL, Haynes CL. Analytical aspects of nanotoxicology. *Anal Chem*. 2016;88(1):451–479. doi:10.1021/acs.analchem.5b04221